

# MPM VALIDATION: SPHERE-CYLINDER IMPACT TESTS: ENERGY BALANCE

B. Banerjee

Department of Mechanical Engineering, University of Utah, Salt Lake City, UT 84112, USA

August 04, 2004

## ABSTRACT

This report discusses the energy balance results observed during the simulation of the impact of an aluminum sphere on an aluminum plate supported by a hollow aluminum cylinder. Due to the high impact velocity, there is considerable ringing of the cylinder which causes the sum of the mechanical energies to increase. An optimal set of input parameters is identified that minimizes ringing and reduces energy increase over the time of the simulation.

## 1 INTRODUCTION

The validation experiments described in this report simulate the impact of a 6061-T6 aluminum sphere against a plate attached to a hollow cylinder of the same material (Chhabildas et al. [1]). The geometry of the experiment and the point of impact are shown in Figure 1. These data correspond to the case L3 described by Chhabildas et al. [1].

The material models and properties used for the simulations are discussed in Section 2. The various models and options used for failure simulation are discussed in Section 3. The approach used for deciding the test sequence is discussed in Section 4. Simulation results are presented and discussed

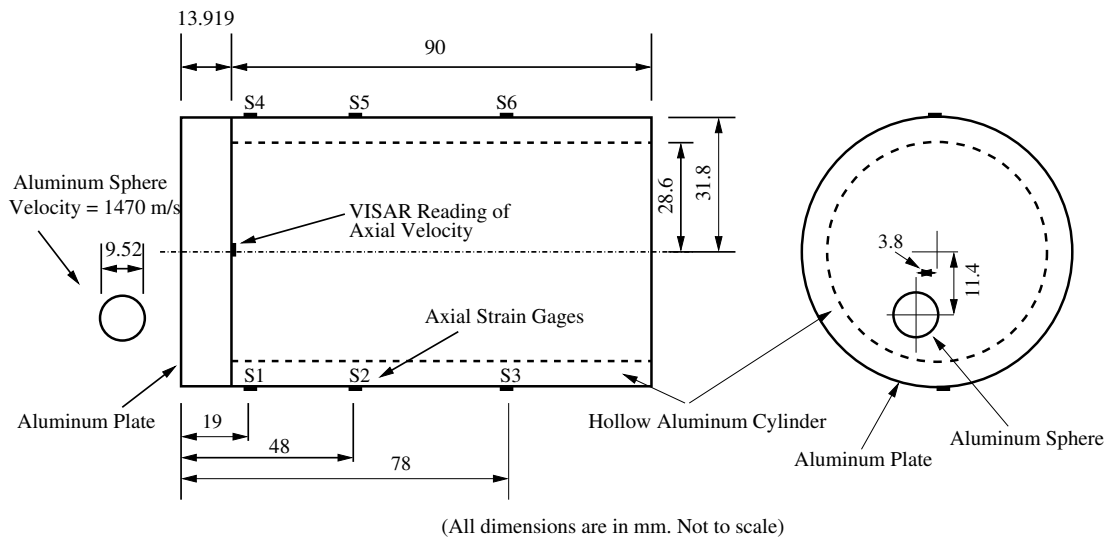


Figure 1: Geometry of cylinder impact tests (L3).

in Section 5.

## 2 MATERIAL MODELS AND PROPERTIES

In the calculations, the Cauchy stress is decomposed into a volumetric and a deviatoric part as shown in equation (1).

$$\boldsymbol{\sigma} = p\mathbf{I} + \mathbf{s} \quad (1)$$

where  $\boldsymbol{\sigma}$  is the Cauchy stress,  $p$  is the hydrostatic pressure,  $\mathbf{I}$  is the second-order identity tensor, and  $\mathbf{s}$  is the deviatoric part of the stress.

The hydrostatic pressure is computed using a hypoelastic constitutive model as shown in equation (2)

$$p_{n+1} = p_n + (K - 2/3\mu) \text{tr}(\mathbf{D})\Delta t \quad (2)$$

where  $p_{n+1}$  is the pressure at time-step  $(n + 1)$ ,  $p_n$  is the pressure at the end of time-step  $(n)$ ,  $\mathbf{D}$  is the rate of deformation tensor,  $K$  is the bulk modulus,  $\mu$  is the shear modulus, and  $\Delta t$  is the time increment. A forward Euler time stepping scheme is used. An alternative way of computing the hydrostatic pressure is to use a Mie-Gruneisen type of equation of state (Zocher et al. [2]) as shown in equation (3)

$$-p = \frac{\rho_0 C_0^2 \zeta \left[1 + \left(1 - \frac{\Gamma_0}{2}\right) \zeta\right]}{\left[1 - (S_\alpha - 1)\zeta\right]^2 + \Gamma_0 C_p T}, \quad \zeta = (\rho/\rho_0 - 1) \quad (3)$$

where  $C_0$  is the bulk speed of sound,  $\rho_0$  is the initial density,  $\rho$  is the current density,  $C_p$  is the specific heat at constant volume,  $T$  is the temperature,  $\Gamma_0$  is the Gruneisen gamma at reference state, and  $S_\alpha$  is the linear Hugoniot slope coefficient.

The deviatoric stress is computed using a hypoelastic stress update that uses a forward Euler time discretization for the elastic domain and a semi-implicit stress update (Maudlin and Schiferl [3]) for the plastic domain. The procedure used for the forward Euler updated of the elastic deviatoric stresses is shown in equation (4)

$$\mathbf{s}_{n+1} = \mathbf{s}_n + 2 \text{dev}(\mathbf{D})\mu\Delta t \quad (4)$$

where  $\mathbf{s}_{n+1}$  is the deviatoric stress at time-step  $(n + 1)$ ,  $\mathbf{s}_n$  is the deviatoric stress at the end of time-step  $(n)$ ,  $\text{dev}(\mathbf{D})$  is the deviatoric part of the rate of deformation tensor,  $\mu$  is the current shear modulus, and  $\Delta t$  is the time increment.

For the plastic part of the stress update, the flow stress is computed using the Johnson-Cook model (Johnson and Cook [4]) shown in equation (5)

$$\sigma_f = [A + B(\epsilon_p)^n][1 + C \ln(\dot{\epsilon}_p^*)][1 - (T^*)^m]; \quad \dot{\epsilon}_p^* = \frac{\dot{\epsilon}_p}{\dot{\epsilon}_{p0}}; \quad T^* = \frac{(T - T_r)}{(T_m - T_r)} \quad (5)$$

where  $\sigma_f$  is the flow stress,  $\dot{\epsilon}_{p0}$  is a user defined plastic strain rate,  $A$ ,  $B$ ,  $C$ ,  $n$ ,  $m$  are material constants,  $T$  is the local temperature of the material,  $T_r$  is the room temperature, and  $T_m$  is the melt temperature. The von-Mises yield condition is used to determine if a trial stress state is inside or outside the yield surface. The function used is shown in equation (6)

$$\Phi = \left(\frac{\sigma_{eq}}{\sigma_f}\right)^2 - 1 = 0; \quad \sigma_{eq} = \sqrt{\frac{3}{2} \text{dev}(\boldsymbol{\sigma}) : \text{dev}(\boldsymbol{\sigma})} \quad (6)$$

where  $\sigma_{eq}$  is the von Mises equivalent stress,  $\sigma^f$  is the flow stress, and  $\text{dev}(\boldsymbol{\sigma})$  is the deviatoric part of the Cauchy stress. The trial stress is projected on to the yield surface using a radial return algorithm (Maudlin and Schiferl [3]).

A scalar damage parameter is computed using the Johnson-Cook damage model (Johnson and Cook [5]). The damage evolution rule for the Johnson-Cook damage model is shown in equation (7)

$$\dot{D} = \frac{\dot{\epsilon}_p}{\epsilon_p^f}; \quad \epsilon_p^f = \left[ D_1 + D_2 \exp\left(\frac{D_3}{3}\sigma^*\right) \right] [1 + D_4 \ln(\dot{\epsilon}_p^*)] [1 + D_5 T^*]; \quad \sigma^* = \frac{\text{tr}(\boldsymbol{\sigma})}{\sigma_{eq}}; \quad (7)$$

where  $D$  is the damage variable which has a value of 0 for virgin material and a value of 1 at fracture,  $\epsilon_p^f$  is the fracture strain,  $D_1, D_2, D_3, D_4, D_5$  are constants,  $\boldsymbol{\sigma}$  is the Cauchy stress, and  $T^*$  is the scaled temperature used in the Johnson-Cook plasticity model.

Part of the plastic work done is converted into heat and used to update the temperature of a particle. The increase in temperature ( $\Delta T$ ) due to an increment in plastic strain ( $\Delta \epsilon_p$ ) is shown in equation (8) (Borvik et al. [6])

$$\Delta T = \frac{\chi \Delta t}{\rho C_p} \boldsymbol{\sigma} : \mathbf{D} \quad (8)$$

where  $\chi$  is the Taylor-Quinney coefficient, and  $C_p$  is the specific heat. It is assumed that the process is adiabatic within a time-step.

The material properties used in the simulations are shown in Table 1. The bulk properties of the 6061-T6 Aluminum alloy were obtained from the Material Web website. The Johnson-Cook plasticity and damage model data were obtained from Lesuer et al. [7]. The Mie-Gruneisen equation of state parameters were obtained from data used in ALEGRA (Chhabildas et al. [1]).

Table 1: Material properties of 6061-T6 Aluminum alloy.

Density	2700	kg/m <sup>3</sup>	<a href="http://www.matweb.com">http://www.matweb.com</a>
Shear Modulus	26	GPa	<a href="http://www.matweb.com">http://www.matweb.com</a>
Bulk Modulus	66.4	GPa	<a href="http://www.matweb.com">http://www.matweb.com</a>
Thermal Conductivity	166.9	W/m-K	<a href="http://www.matweb.com">http://www.matweb.com</a>
Specific Heat	896	J/kg-K	<a href="http://www.matweb.com">http://www.matweb.com</a>
Melting Temperature	925	K	Lesuer et al. [7]
Room Temperature	294	K	
Johnson-Cook A	324	MPa	Lesuer et al. [7]
Johnson-Cook B	114	MPa	Lesuer et al. [7]
Johnson-Cook C	0.002		Lesuer et al. [7]
Johnson-Cook n	0.42		Lesuer et al. [7]
Johnson-Cook m	1.34		Lesuer et al. [7]
Johnson-Cook D <sub>1</sub>	-0.77		Lesuer et al. [7]
Johnson-Cook D <sub>2</sub>	1.45		Lesuer et al. [7]
Johnson-Cook D <sub>3</sub>	-0.47		Lesuer et al. [7]
Johnson-Cook D <sub>4</sub>	0		Lesuer et al. [7]
Johnson-Cook D <sub>5</sub>	1.6		Lesuer et al. [7]
Mie-Gruneisen C <sub>0</sub>	5386	m/s	ALEGRA input deck
Mie-Gruneisen $\Gamma_0$	1.99		ALEGRA input deck
Mie-Gruneisen S <sub><math>\alpha</math></sub>	1.339		ALEGRA input deck
Taylor-Quinney Coefficient $\chi$	0.9		Farren and Taylor [8], Quinney and Taylor [9]

### 3 FAILURE SIMULATION

The determination of whether a particle has failed can be made on the basis of either or all of the following conditions:

- The particle temperature exceeds the melting temperature. This is specified by the `do_melting` option.
- The TEPLA-F fracture condition (Johnson and Addessio [10]) is satisfied.
- A bifurcation condition is satisfied.

The TEPLA-F condition can be written as shown in equation (9)

$$(f/f_c)^2 + (\epsilon_p/\epsilon_p^f)^2 = 1 \quad (9)$$

where  $f$  is the current porosity,  $f_c$  is the maximum allowable porosity,  $\epsilon_p$  is the current plastic strain, and  $\epsilon_p^f$  is the plastic strain at fracture. In these simulations, the porosity was kept constant at a zero value.

The bifurcation conditions used for the simulations are the Drucker stability postulate (Drucker [11]) and the loss of hyperbolicity condition (Rudnicki and Rice [12], Perzyna [13]). The Drucker stability postulate states that rate of change of the rate of work done by a material cannot be negative. Therefore, the material is assumed to become unstable (and a particle fails) when

$$\dot{\sigma} : \mathbf{D}^p \leq 0 \quad (10)$$

The loss of hyperbolicity criterion states that the material loses stability if the determinant of the acoustic tensor changes sign (Rudnicki and Rice [12], Perzyna [13]). Determination of the acoustic tensor requires a search for a normal vector around the material point and is therefore computationally expensive. A simplification of this criterion is a check which assumes that the direction of instability lies in the plane of the maximum and minimum principal stress (Becker [14]). In this approach, we assume that the strain is localized in a band with normal  $\mathbf{n}$ , and the magnitude of the velocity difference across the band is  $\mathbf{g}$ . Then the bifurcation condition leads to the relation

$$R_{ij}g_j = 0; \quad R_{ij} = M_{ikjl}n_kn_l + M_{ilkj}n_kn_l - \sigma_{ik}n_jn_k \quad (11)$$

where  $M_{ijkl}$  are the components of the co-rotational tangent modulus tensor and  $\sigma_{ij}$  are the components of the co-rotational stress tensor. If  $\det(R_{ij}) \leq 0$ , then  $g_j$  can be arbitrary and there is a possibility of strain localization. If this condition for loss of hyperbolicity is met, then a particle deforms in an unstable manner and failure can be assumed to have occurred at that particle.

When a particle has failed, it is assigned a flag and may be assigned to a different material with a new velocity field (option `create_new_particles`). In addition, the stress state might be modified. When the option `erosion_algorithm` "none" is chosen, none of the tests for failure (except melting) are carried out and nothing is done to alter the stress state in the particles. However, if the option `do_melting` is chosen, the deviatoric stress is set to zero upon melting even if no erosion algorithm has been chosen. If the erosion algorithm is "AllowNoTension" then tensile states of hydrostatic stress are set to zero. If the erosion algorithm type is set to "KeepStress" the stress state is maintained. If the erosion algorithm type is "ZeroStress", the stress is failed particles is set to zero and maintained at that value.

An artificial viscosity was optionally used to damp the internal forces used in the balance of momentum equation. The equations used to calculate the artificial bulk viscosity ( $q$ ) are shown

below (VonNeumann and Richtmyer [15], Wilkins [16])

$$q = \begin{cases} \rho(C_L|aD_{kk}l| + C_0D_{kk}^2l^2) & \text{if } D_{kk} < 0, \\ 0 & \text{if } D_{kk} \geq 0 \end{cases} \quad (12)$$

where  $\rho$  is the current density,  $l = (\Delta x + \Delta y + \Delta z)/3$  is the characteristic length,  $C_L$  is the linear damping coefficient (default = 0.2),  $C_0$  is the quadratic damping coefficient (default = 2.0),  $a = \sqrt{K/\rho}$  is the local bulk sound speed, and  $D_{kk}$  is the trace of rate of deformation tensor.

In addition, contact between bodies can be achieved either using a friction contact algorithm or an approach contact algorithm. Also, interpolation from the particles to the background mesh and back can be performed using a 8-point or a 27-point method.

#### 4 APPROACH

A series of tests was performed to determine the set of inputs that led to the best mechanical energy conservation behavior with all features relevant to the problem turned on. The input XML file corresponding to that case is shown in Appendix I. Twelve more cases were run with a feature turned off or changed and the energy balance was observed up to a run time of 40  $\mu s$ . Beyond this time the energy change was negligible.

The parameters that were changed in the simulations are listed in Table 2. Previous validation tests using Taylor impact specimens without particle erosion (at lower initial velocities) had shown that mechanical energy was conserved very well. Hence, the increase in total mechanical energy was to be associated with processes that occur at high velocities such as shocks (artificial viscosity is required to smooth out the shock front), melting, and particle failure. The contact algorithm was varied because particles interact via contact after failure when the `create_new_particles` is turned on.

#### 5 RESULTS

The energy balance for each of the cases listed in Table 2 is compared with that for Case 1 and the results are discussed below. The figures show the sum of the kinetic energy of all the particles varying with time, calculated using the equation

$$KE = \frac{1}{2}mv^2 \quad (13)$$

where  $m$  is the mass of the particle and  $v$  is the updated velocity of the particle at the end of a time-step. The total accumulated strain energy summed over all particles is also shown as a function of time. The increment of strain energy of a particle at the end of a time-step is calculated using the equation

$$\Delta SE = (\boldsymbol{\sigma} : \mathbf{D})V\Delta t ; \quad \boldsymbol{\sigma} = \frac{1}{2}(\boldsymbol{\sigma}_{n+1} + \boldsymbol{\sigma}_n) \quad (14)$$

where  $\boldsymbol{\sigma}_{n+1}$  is the Cauchy stress at the end of the time-step,  $\boldsymbol{\sigma}_n$  is the stress at the beginning of the time-step,  $\mathbf{D}$  is the rate of deformation tensor,  $V$  is the volume at the end of the time-step, and  $\Delta t$  is the time increment. The total energy shown in the figures is the sum of the kinetic energy and the accumulated strain energy of the particles as a function of time.

##### 5.1 Case 2: Effect of change in initial time-step size

Figure 2(a) shows the energy plot for Case 1 while Figure 2(b) shows the energy plot for Case 2. Though it is not obvious from the figure, the final total energy for Case 2 is slightly more than 1400

J and increases faster than that in Case 1. It has also been observed (from other runs) that if the minimum time-step increment is set to less than  $5 \times 10^{-8}$  s, the simulation become unstable and the kinetic energy increases by more than two orders of magnitude. This behavior is probably due to the accumulation of floating point errors. Care needs to be exercised to see that excessively small time steps are not used in the simulation.

### 5.2 Case 3: Effect of change in artificial viscosity parameters

Figures 3(a) and 3(b) show the energy balance change with change in the artificial viscosity parameters. Even though the change in the parameters is small, the total energy change is significant. For the parameters used in Case 3, the total energy increases to more than 1450 J compared to 1400 J for Case 1. The simulations are therefore quite sensitive to changes in the viscosity parameters and these parameters should be chosen with care.

### 5.3 Case 4: Effect of turning off artificial viscosity

Figures 4(a) and 4(b) show the energy balance with and without artificial viscosity turned on. In the reference case (Case 1), artificial viscosity is on and the initial fluctuations in energy are dampened out considerably. The final total energy is less than 1400 J. However, when artificial viscosity is turned off, there are large variations in the initial total energy before a steady value of around 1520 J is attained. If approach contact is used with artificial viscosity turned off, the total energy remains at the peak value attained which is around 1700 J. For lower velocity impacts, the initial ringing is not as pronounced. However, artificial viscosity needs to be incorporated into high velocity impact simulations to avoid serious increases in the kinetic energy which can lead to spurious results.

Table 2: Parameters varied in the simulations.

Case	Parameters Changed	Old Values (Case1)	New Values
2	Initial $\Delta t$	$10^{-7}$ s	$10^{-11}$ s
3	Artificial Viscosity Coeffs		
	$C_L$	0.07	0.06
	$C_0$	1.6	1.5
4	Artificial Viscosity Flag	on	off
5	Create Particles Flag	on	off
6	Erosion Algorithm Flag	AllowNoTension	none
7	Erosion Algorithm Flag	AllowNoTension	none
	Do Melting	on	off
8	Erosion Algorithm Flag	AllowNoTension	KeepStress
9	Erosion Algorithm Flag	AllowNoTension	KeepStress
	Do Melting	on	off
10	Contact Type	friction	approach
11	Initial Velocity	1470 m/s	700 m/s
12	Nodes used in interpolation	27	8
13	Equation of state	Hypoelastic	Mie-Gruneisen
14	Timestep Multiplier	0.8	0.1
15	Contact Type	friction	single_velocity
16	Contact Type	friction	single_velocity
	Timestep Multiplier	0.8	0.1

#### 5.4 Case 5: Effect of turning off particle creation

When the `create_new_particles` flag is turned on, failed particles are converted into a new material with the same properties. This new material interacts with the rest of the body via contact. Figure 5(a) shows the energy balance when particle creation is turned on. The energy plot for the case where particle creation is turned off is shown in Figure 5(b). The initial energy fluctuations are smaller when particle creation is turned off. However, the total energy continues to increase with time and reaches a higher final value than in the reference case. The reference case is preferable as far as energy conservation is concerned.

#### 5.5 Case 6: Effect of turning off erosion

The option `<erosion algorithm = "none" />` turns off the mechanism that computes whether a particle has failed. However, melted particles are still flagged and the deviatoric stress in those particles are set to zero. Figures 6(a) and 6(b) show the energy plots with and without erosion turned on, respectively. When erosion is turned off, increased dissipation is observed due to artificial viscosity. However, the initial fluctuations in the total energy remain which implies that particle erosion is not the cause of the fluctuations.

#### 5.6 Case 7: Effect of turning off erosion and melting

Figure 7(b) shows the energy balance when, in addition to particle erosion, melting is turned off. There is no significant difference between Figure 6(b) and Figure 7(b). We conclude that initial melting does not play a significant role in the energy balance.

#### 5.7 Case 8: Effect of changing erosion algorithm

The erosion algorithm used in the reference calculation (Case 1) is `AllowNoTension`. In that case, tensile hydrostatic stresses are not allowed for failed particles. Figure 8(a) shows the energy balance for the reference case. Figure 8(b) shows the energy balance when the erosion algorithm is changed to `KeepStres`. In this case, the failed particles retain their stresses and evolve by relaxation. This option is appropriate when particle creation is turned on so that surface creation is simulated instead of particle failure. The figures show that the energy balance is much better behaved than in the reference case. Hence, this is one of the options chosen for the detailed simulations.

#### 5.8 Case 9: Effect of changing erosion algorithm and melting

In this case, the `KeepStress` erosion algorithm is used and melting is turned off so that particle stresses are not modified in any way upon failure but transferred to the newly created particles. Figure 9(b) shows the energy balance for this case compared to that for the reference case shown in Figure 9(a). If we compare Figure 9(b) with Figure 8(b), the difference between the two is not significant. This further reinforces the conclusion that the melted particles do contribute significantly to the energy balance.

#### 5.9 Case 10: Effect of changing contact algorithm

During some of our computations we have observed that for certain geometries particles do not see each other accurately when friction contact (as devised by Bardenhagen et al. [17]) is used. Approach contact is often more appropriate for these geometries. Figure 10(a) shows the energy evolution with time when a friction contact algorithm is used with a coefficient of friction of 0.0001 (the reference case). Figure 10(b) shows energy when an approach contact algorithm is used. The total energy increases considerably when the approach contact algorithm is used. These results suggest that improvements could be made to the approach contact algorithm. We already know that the friction contact algorithm fails in certain cases. Hence, a new contact algorithm for failed particles may be necessary.

### 5.10 Case 11: Effect of change in impact velocity

The results seen so far suggest that the initial fluctuations in the total energy are due to the high velocity of impact. Figures 11(a) and (b) show energy plots for high and low velocity impacts, respectively. The lower velocity impact shows smaller initial fluctuations and a decrease in total energy consistent with the use of artificial viscous damping. If viscous damping is turned off, energy is conserved quite well and initial fluctuations remain small. These results seem to confirm that the increase in energy is caused by ringing due to the high velocity of impact in the reference case.

### 5.11 Case 12: Effect of change in interpolation order

The standard MPM algorithm (Sulsky et al. [18, 19]) uses a 8-node interpolation. Instabilities were found to occur at large deformations when this algorithm was used and a 27-node interpolation algorithm was devised by Bardenhagen and Kober [20]. Figure 12(a) shows the energy plot for the reference case that uses 27-node interpolation while Figure 12(b) shows the energy balance for 8-node interpolation. The increase in total energy is higher for 8-node interpolation. This result further confirms the improved performance of 27-node interpolation.

### 5.12 Case 13: Effect of changing equation of state

If the reference simulation, a hypoelastic constitutive model was used to compute the hydrostatic pressure. If the Mie-Gruneisen equation of state is used instead, we see a marked increase in the total energy as shown in Figures 13(a) and (b). The difference is probably due to the incorrect calculation of the internal energy that is used in the Mie-Gruneisen equation of state. The current implementation approximates the internal energy as

$$E = C_p T \quad (15)$$

where  $E$  is the internal energy,  $C_p$  is the specific heat, and  $T$  is the temperature. Efforts are underway to improve the algorithm and observe the effect of the changes on the energy balance.

### 5.13 Case 14: Effect of changing timestep multiplier

The stability of a forward Euler time integration is supposed to increase with decrease in the time step. The results in Case 1 contradicted this known property of the time discretization scheme. To further confirm this we ran a case with a timestep multiplier of 0.1 instead of 0.8 in the reference case. We also looked at the momentum to see if conservation was being achieved. Figure 14 shows the energy and momentum comparisons for this case. Both the energy and momentum increase with time for the lower timestep size. We suspect that the friction contact algorithm is leading to this instability. We also observe that momentum is not conserved in the reference case.

### 5.14 Case 15: Effect of applying single velocity contact

The results from the previous section led us to suspect that friction contact was causing spurious momentum gains. These gains have not observed in lower velocity impacts implying that the magnitude of the initial velocities can make the contact algorithm unstable. In order to demonstrate that our hunch is indeed correct, we have run a case with `single_velocity` contact - the standard contact algorithm in MPM. Figure 15 shows the evolution of energy and momentum for this case. As before, the figures on the left represent the reference case. Both the energy and momentum balance are better behaved in the single velocity contact case. However, there is a slight increase in momentum with time.

### 5.15 Case 16: Effect of applying single velocity contact with lower timestep multiplier

In order to confirm that there is nothing inherent in the code that leads to the increase in energy and momentum with lower timestep sizes (see Figure 14), we ran another case with single velocity contact and a low timestep. The results for this case are shown in Figure 16. The results confirm that the friction contact algorithm causes the energy and momentum to increase dramatically for low timestep multipliers. It is also seen that momentum is almost exactly conserved though there is some decrease in energy. The energy decrease is due to the `AllowNoTension` option. If the `KeepStress` option is used, energy is also conserved very accurately when timestep multipliers less than 0.2 are used.

## 6 CONCLUSION

From the energy balance results, we conclude that the best results should be obtained using the reference case with the erosion algorithm changed to `KeepStress`. The contact algorithm should be changed to `single_velocity` and the timestep multiplier should be less than 0.2. All other options tend to increase the total energy and do not conserve momentum and could lead to spurious results.

## ACKNOWLEDGMENTS

This work was supported by the the U.S. Department of Energy through the Center for the Simulation of Accidental Fires and Explosions, under grant W-7405-ENG-48.

## REFERENCES

- [1] Chhabildas, L. C., Konrad, C. H., Mosher, D. A., Reinhart, W. D., Duggins, B. D., Trucano, T. G., Summers, R. M., and Peery, J. S. A methodology to validated 3D arbitrary Lagrangian Eulerian codes with applications to ALEGRA. *Int. J. Impact Engrg.*, 23:101–112, 1998.
- [2] Zocher, M. A., Maudlin, P. J., Chen, S. R., and Flower-Maudlin, E. C. An evaluation of several hardening models using Taylor cylinder impact data. In *Proc. , European Congress on Computational Methods in Applied Sciences and Engineering*, Barcelona, Spain, 2000. ECCOMAS.
- [3] Maudlin, P. J. and Schiferl, S. K. Computational anisotropic plasticity for high-rate forming applications. *Comput. Methods Appl. Mech. Engrg.*, 131:1–30, 1996.
- [4] Johnson, G. R. and Cook, W. H. A constitutive model and data for metals subjected to large strains, high strain rates and high temperatures. In *Proc. 7th International Symposium on Ballistics*, pages 541–547, 1983.
- [5] Johnson, G. R. and Cook, W. H. Fracture characteristics of three metals subjected to various strains, strain rates, temperatures and pressures. *Int. J. Eng. Fract. Mech.*, 21:31–48, 1985.
- [6] Borvik, T., Hopperstad, O. S., Berstad, T., and Langseth, M. A computational model of viscoplasticity and ductile damage for impact and penetration. *Eur. J. Mech. A/Solids*, 20:685–712, 2001.
- [7] Lesuer, D. R., Kay, G. J., and LeBlanc, M. M. Modeling large-strain, high-rate deformation in metals. Technical Report UCRL-JC-134118, Lawrence Livermore National Laboratory, Livermore, CA, 2001.
- [8] Farren, W. S. and Taylor, G. I. The heat developed during plastic extension of metals. *Proc. Royal Soc. Lond. A*, 107 (743):422–451, 1925.
- [9] Quinney, H. and Taylor, G. I. The emission of latent energy due to previous cold working when a metal is heated. *Proc. Royal Soc. Lond. A*, 163(913):157–181, 1937.
- [10] Johnson, J. N. and Addessio, F. L. Tensile plasticity and ductile fracture. *J. Appl. Phys.*, 64(12):6699–6712, 1988.
- [11] Drucker, D. C. A definition of stable inelastic material. *J. Appl. Mech.*, 26:101–106, 1959.
- [12] Rudnicki, J. W. and Rice, J. R. Conditions for the localization of deformation in pressure-sensitive dilatant materials. *J. Mech. Phys. Solids*, 23:371–394, 1975.
- [13] Perzyna, P. Constitutive modelling of dissipative solids for localization and fracture. In P., P., editor, *Localization and Fracture Phenomena in Inelastic Solids: CISM Courses and Lectures No. 386*, pages 99–241. SpringerWien, New York, 1998.
- [14] Becker, R. Ring fragmentation predictions using the guron model with material stability conditions as failure criteria. *Int. J. Solids Struct.*, 39:3555–3580, 2002.
- [15] VonNeumann, J. and Richtmyer, R. D. A method for the numerical calculation of hydrodynamic shocks. *J. Appl. Phys.*, 21:232, 1950.

- [16] Wilkins, M. L. Calculation of elastic-plastic flow. In Alder, B., Fernbach, S., and Rotenberg, M., editors, *Methods in Computational Physics V.3*, pages 211–263. Academic Press, New York, 1964.
- [17] Bardenhagen, S. G., Guilkey, J. E., Roessig, K. M., BrackBill, J. U., Witzel, W. M., and Foster, J. C. An improved contact algorithm for the material point method and application to stress propagation in granular material. *Computer Methods in the Engineering Sciences*, 2(4):509–522, 2001.
- [18] Sulsky, D., Chen, Z., and Schreyer, H. L. A particle method for history dependent materials. *Comput. Methods Appl. Mech. Engrg.*, 118:179–196, 1994.
- [19] Sulsky, D., Zhou, S., and Schreyer, H. L. Application of a particle-in-cell method to solid mechanics. *Computer Physics Communications*, 87:236–252, 1995.
- [20] Bardenhagen, S. G. and Kober, E. M. The generalized interpolation material point method. *Comp. Model. Eng. Sci.*, 2004. to appear.

## APPENDIX I. INPUT FILE : CASE 1

```
<?xml version='1.0' encoding='ISO-8859-1' ?>
<!-- @version: -->
<Uintah_specification>

<!-- 6061 T6 Al Sphere impacting 6061 T6 Al Cylinder,
      Hypoelastic stress update,
      Johnson Cook Plasticity Model, Johnson Cook Damage Model,
      Default Hypoelastic Equation of State -->

<Meta>
  <title>Sphere Impacting Cylinder</title>
</Meta>

<Time>
  <maxTime>          40.0e-6    </maxTime>
  <initTime>         0.0        </initTime>
  <delt_min>         0.0        </delt_min>
  <delt_max>         1e-5       </delt_max>
  <delt_init>        1e-7       </delt_init>
  <timestep_multiplier> 0.8      </timestep_multiplier>
</Time>

<DataArchiver>
  <filebase>impactAlSphCylSmEroJCL3Tiny.uda</filebase>
  <outputInterval> 1.0e-6 </outputInterval>
  <compression>gzip</compression>
  <outputDoubleAsFloat/>
  <save label = "p.particleID"/>
  <save label = "p.x"/>
  <save label = "p.stress"/>
  <save label = "p.velocity"/>
  <save label = "p.deformationMeasure"/>
  <save label = "p.localized"/>
  <save label = "AccStrainEnergy"/>
  <save label = "KineticEnergy"/>
  <save label = "ThermalEnergy"/>
  <checkpoint cycle = "2" timestepInterval = "100"/>
</DataArchiver>

<MPM>
  <time_integrator>explicit</time_integrator>
  <nodes8or27>          27      </nodes8or27>
  <minimum_particle_mass> 1.0e-8 </minimum_particle_mass>
  <maximum_particle_velocity> 1.0e8 </maximum_particle_velocity>
  <artificial_damping_coeff> 0.0 </artificial_damping_coeff>
  <artificial_viscosity> true </artificial_viscosity>
  <artificial_viscosity_coeff1> 0.07 </artificial_viscosity_coeff1>
  <artificial_viscosity_coeff2> 1.6 </artificial_viscosity_coeff2>
  <accumulate_strain_energy> true </accumulate_strain_energy>
  <turn_on_adiabatic_heating> false </turn_on_adiabatic_heating>
  <use_load_curves> false </use_load_curves>
  <create_new_particles> true </create_new_particles>
  <erosion algorithm = "AllowNoTension"/>
</MPM>

<PhysicalConstants>
  <gravity>          [0,0,0] </gravity>
  <reference_pressure> 101325.0 </reference_pressure>
```

```

</PhysicalConstants>

<MaterialProperties>
  <MPM>
    <material>
      <density> 2700.0 </density>
      <toughness> 29.e6 </toughness>
      <thermal_conductivity> 166.9 </thermal_conductivity>
      <specific_heat> 896.0 </specific_heat>
      <room_temp> 294.0 </room_temp>
      <melt_temp> 925.0 </melt_temp>
      <constitutive_model type = "elastic_plastic">
        <tolerance> 1.0e-15 </tolerance>
        <useModifiedEOS> true </useModifiedEOS>
        <evolve_porosity> false </evolve_porosity>
        <evolve_damage> true </evolve_damage>
        <compute_specfic_heat> false </compute_specfic_heat>
        <do_melting> true </do_melting>
        <check_TEPLA_failure_criterion> true </check_TEPLA_failure_criterion>
        <shear_modulus> 26.0e9 </shear_modulus>
        <bulk_modulus> 66.4e9 </bulk_modulus>
        <equation_of_state type = "default_hypo"> </equation_of_state>
        <plasticity_model type = "johnson_cook">
          <A> 324.0e6 </A>
          <B> 114.0e6 </B>
          <C> 0.002 </C>
          <n> 0.42 </n>
          <m> 1.34 </m>
        </plasticity_model>
        <yield_condition type = "vonMises"> </yield_condition>
        <stability_check type = "drucker_becker"> </stability_check>
        <damage_model type = "johnson_cook">
          <D1> -0.77 </D1>
          <D2> 1.45 </D2>
          <D3> -0.47 </D3>
          <D4> 0.0 </D4>
          <D5> 1.60 </D5>
        </damage_model>
      </constitutive_model>
      <geom_object>
        <sphere label = "sphere">
          <origin>[9.75e-3, 11.4e-3, -3.8e-3]</origin>
          <radius> 4.75e-3 </radius>
        </sphere>
        <res>[2,2,2]</res>
        <velocity>[1470.0,0.0,0.0]</velocity>
        <temperature>294</temperature>
      </geom_object>
    </material>
    <material>
      <density> 2700.0 </density>
      <toughness> 29.e6 </toughness>
      <thermal_conductivity> 166.9 </thermal_conductivity>
      <specific_heat> 896.0 </specific_heat>
      <room_temp> 294.0 </room_temp>
      <melt_temp> 925.0 </melt_temp>
      <constitutive_model type = "elastic_plastic">
        <tolerance> 1.0e-15 </tolerance>
        <useModifiedEOS> true </useModifiedEOS>

```

```

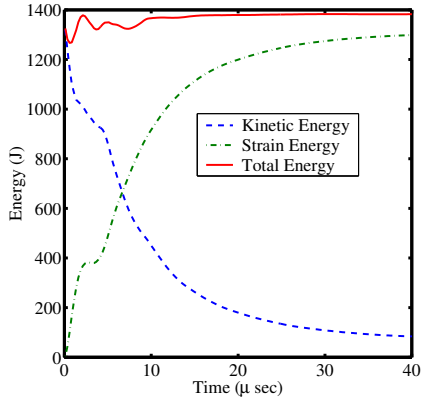
    <evolve_porosity>                false </evolve_porosity>
    <evolve_damage>                  true </evolve_damage>
    <compute_specific_heat>          false </compute_specific_heat>
    <do_melting>                     true </do_melting>
    <check_TEPLA_failure_criterion> true </check_TEPLA_failure_criterion>
    <shear_modulus> 26.0e9 </shear_modulus>
    <bulk_modulus> 66.4e9 </bulk_modulus>
    <equation_of_state type = "default_hypo"> </equation_of_state>
    <plasticity_model type = "johnson_cook">
      <A> 324.0e6 </A>
      <B> 114.0e6 </B>
      <C> 0.002 </C>
      <n> 0.42 </n>
      <m> 1.34 </m>
    </plasticity_model>
    <yield_condition type = "vonMises"> </yield_condition>
    <stability_check type = "drucker_becker"> </stability_check>
    <damage_model type = "johnson_cook">
      <D1> -0.77 </D1>
      <D2> 1.45 </D2>
      <D3> -0.47 </D3>
      <D4> 0.0 </D4>
      <D5> 1.60 </D5>
    </damage_model>
  </constitutive_model>
  <geom_object>
    <smoothcyl label = "end plate">
      <bottom> [15.0e-3, 0.0, 0.0] </bottom>
      <top> [28.919e-3, 0.0, 0.0] </top>
      <radius> 31.8e-3 </radius>
      <num_axial> 10 </num_axial>
      <num_radial> 30 </num_radial>
    </smoothcyl>
    <res>[2,2,2]</res>
    <velocity>[0.0,0.0,0.0]</velocity>
    <temperature>294</temperature>
  </geom_object>
  <geom_object>
    <smoothcyl label = "hollow cylinder">
      <bottom> [28.919e-3, 0.0, 0.0] </bottom>
      <top> [119.0e-3, 0.0, 0.0] </top>
      <radius> 31.8e-3 </radius>
      <thickness> 3.20e-3 </thickness>
      <num_axial> 50 </num_axial>
      <num_radial> 30 </num_radial>
    </smoothcyl>
    <res>[2,2,2]</res>
    <velocity>[0.0,0.0,0.0]</velocity>
    <temperature>294</temperature>
  </geom_object>
</material>
<contact>
  <type>friction</type>
  <mu>0.0001</mu>
  <vel_fields>[0,0,0]</vel_fields>
</contact>
</MPM>
</MaterialProperties>

```

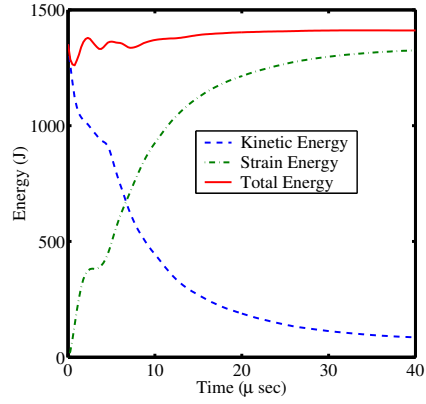
```
<PhysicalBC>
  <MPM>
  </MPM>
</PhysicalBC>

<Grid>
  <Level>
    <Box label = "1">
      <lower>[0.0, -33.0e-3, -33.0e-3]</lower>
      <upper>[119.0e-3, 33.0e-3, 33.0e-3]</upper>
      <patches>[8,1,1]</patches>
      <extraCells>[1,1,1]</extraCells>
      <resolution>[50, 20, 20]</resolution>
    </Box>
  </Level>
  <BoundaryConditions>
    <Face side = "x-">
      <BCType id = "0" label = "Symmetric" var = "symmetry">
      </BCType>
    </Face>
    <Face side = "x+">
      <BCType id = "0" label = "Symmetric" var = "symmetry">
      </BCType>
    </Face>
    <Face side = "y-">
      <BCType id = "0" label = "Symmetric" var = "symmetry">
      </BCType>
    </Face>
    <Face side = "y+">
      <BCType id = "0" label = "Symmetric" var = "symmetry">
      </BCType>
    </Face>
    <Face side = "z-">
      <BCType id = "0" label = "Symmetric" var = "symmetry">
      </BCType>
    </Face>
    <Face side = "z+">
      <BCType id = "0" label = "Symmetric" var = "symmetry">
      </BCType>
    </Face>
  </BoundaryConditions>
</Grid>

</Uintah_specification>
```

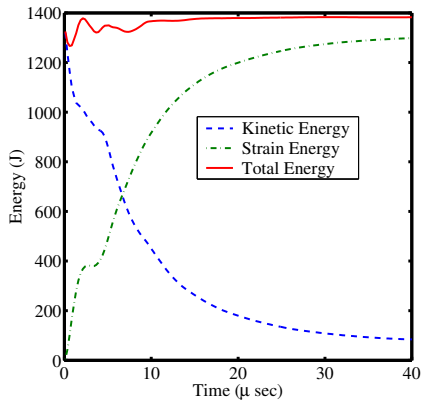


(a) Initial Time-step =  $10^{-7}$  s.

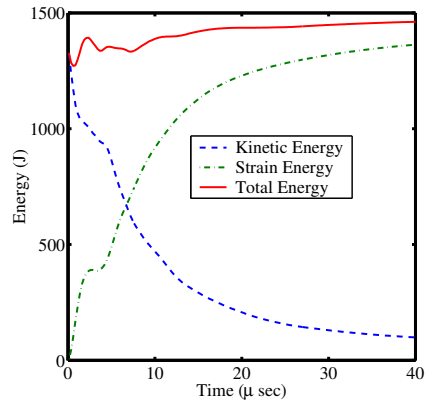


(a) Initial Time-step =  $10^{-11}$  s.

Figure 2: Energy balance before and after initial time step change.

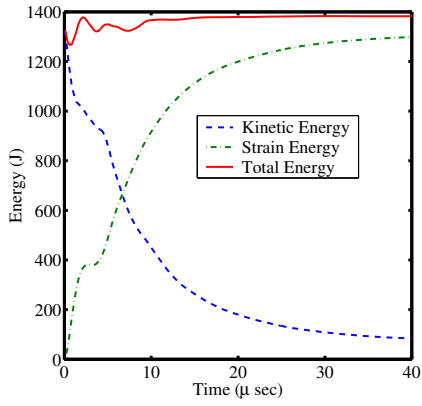


(a)  $C_L = 0.07, C_0 = 1.6$ .

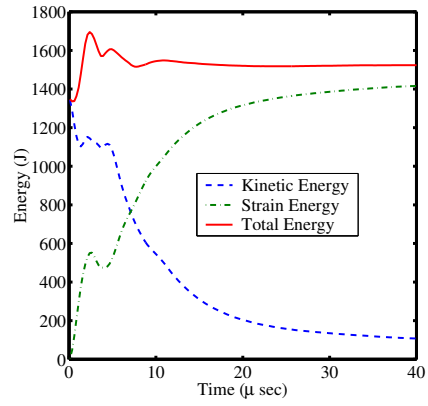


(b)  $C_L = 0.06, C_0 = 1.5$ .

Figure 3: Energy balance before and after change of artificial viscosity parameters.

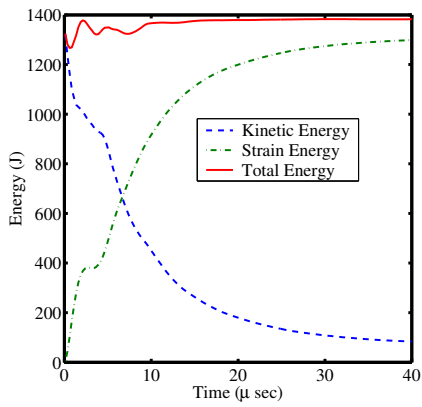


(a) Artificial viscosity turned on.

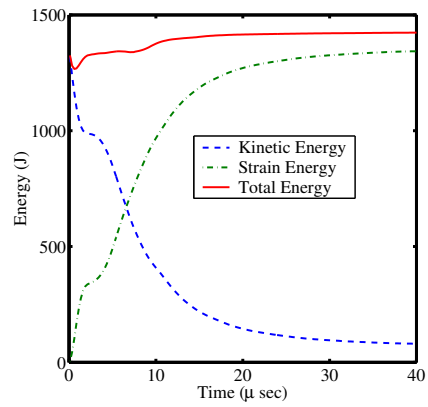


(b) Artificial viscosity turned off.

Figure 4: Energy balance with and without artificial viscosity turned on.

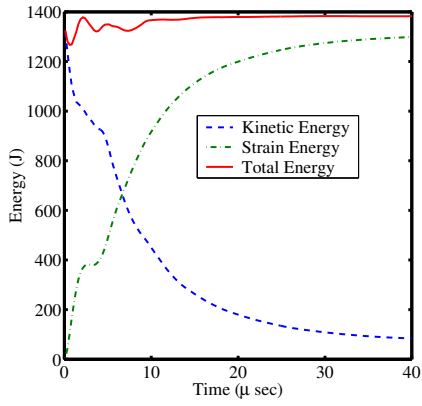


(a) Particle creation turned on.

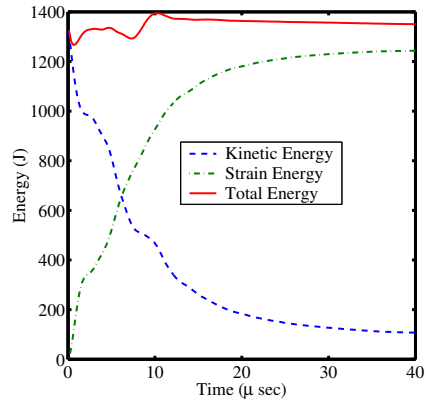


(b) Particle creation turned off.

Figure 5: Energy balance with and without particle creation turned on.

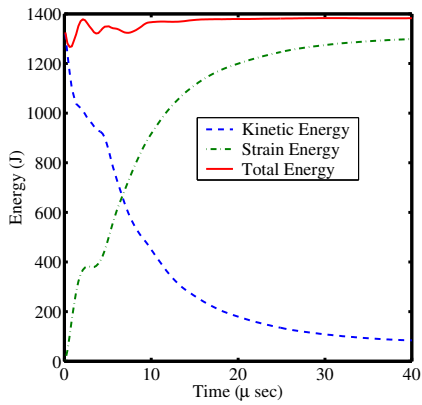


(a) Particle erosion turned on.

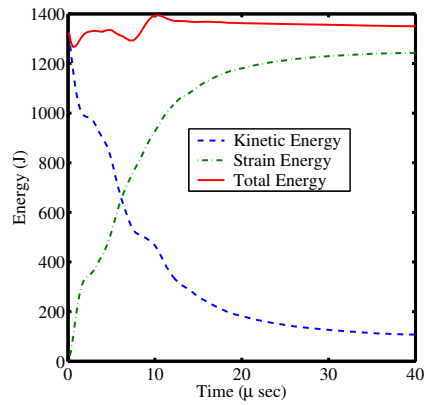


(b) Particle erosion turned off.

Figure 6: Energy balance with and without particle erosion.

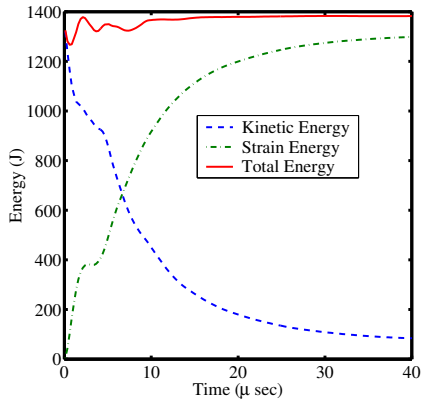


(a) Particle erosion and melting on.

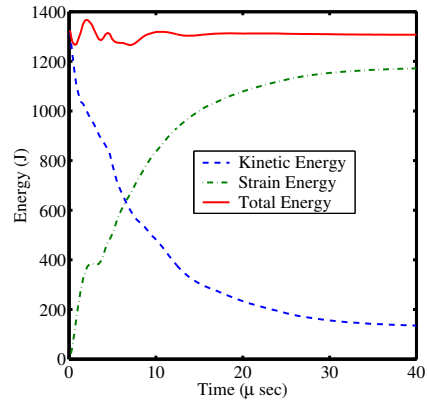


(b) Particle erosion and melting off.

Figure 7: Energy balance with and without particle erosion and melting.

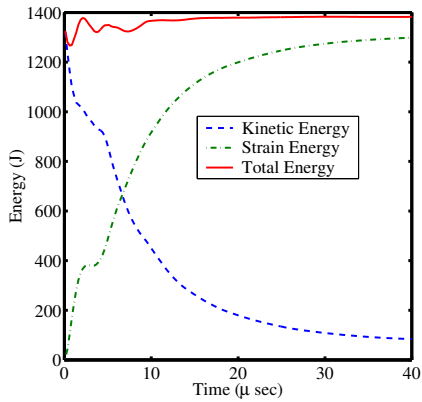


(a) Erosion algorithm AllowNoTension.

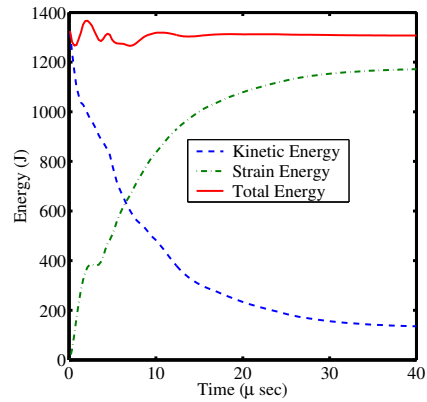


(b) Erosion algorithm KeepStress.

Figure 8: Energy balance before and after change of erosion algorithm.

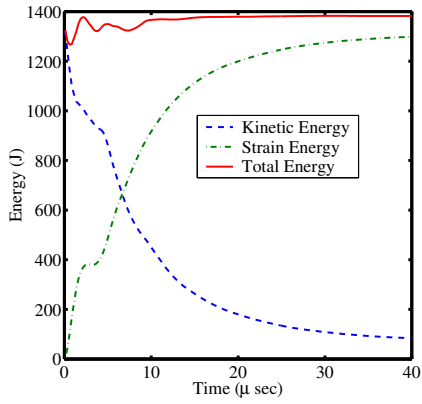


(a) Erosion algorithm AllowNoTension with melting.

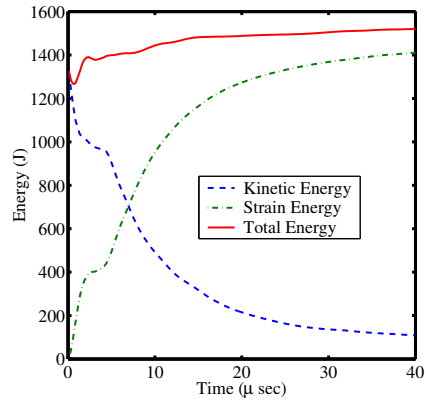


(b) Erosion algorithm KeepStress without melting.

Figure 9: Energy balance before and after change of erosion algorithm and with and without melting.

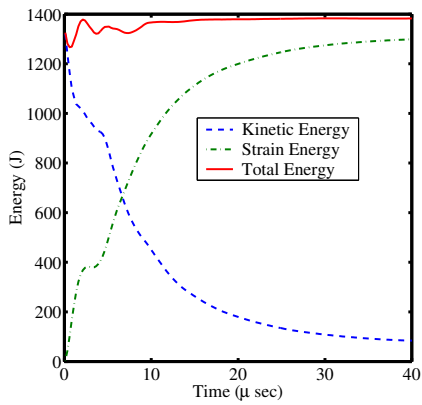


(a) Friction contact.

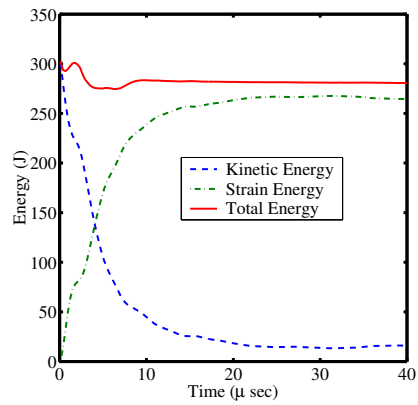


(b) Approach contact.

Figure 10: Energy balance before and after change of contact algorithm.

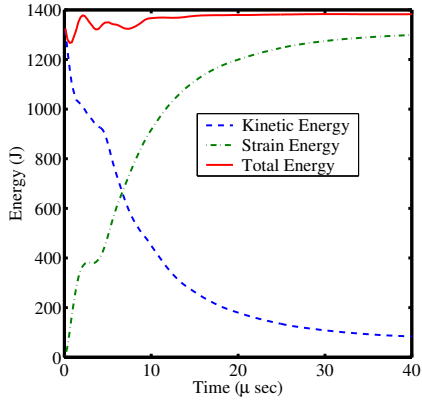


(a) Impact velocity = 1470 m/s.

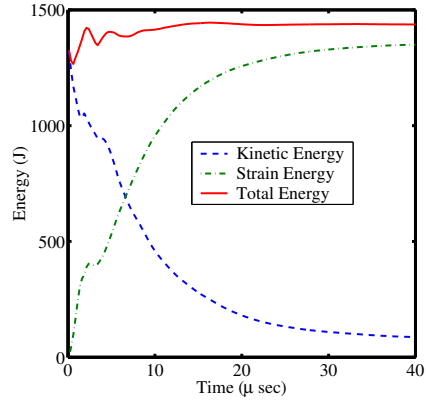


(b) Impact velocity = 700 m/s.

Figure 11: Energy balance before and after change of impact velocity.

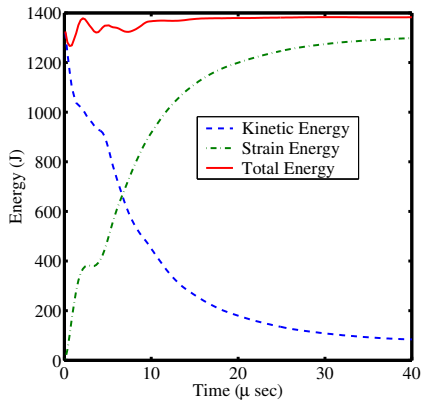


(a) 27-node interpolation.

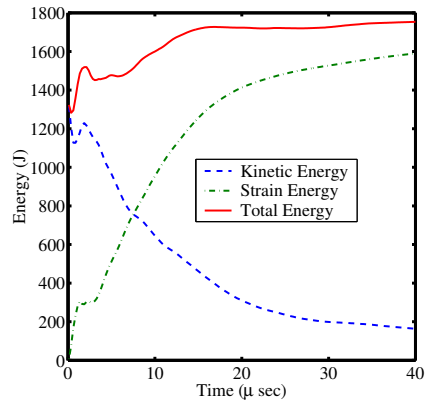


(b) 8-node interpolation.

Figure 12: Energy balance for different interpolation methods.

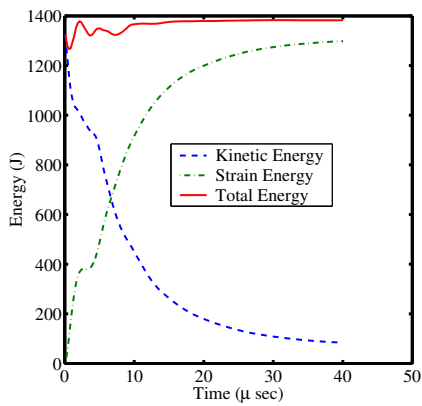


(a) Without EOS.

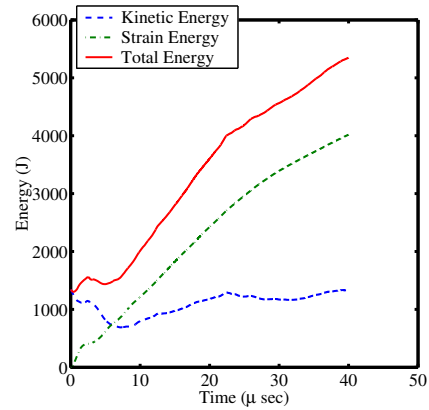


(b) With Mie-Gruneisen EOS.

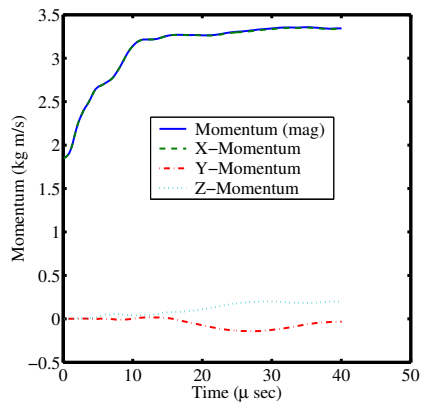
Figure 13: Energy balance with and without Mie-Gruneisen EOS.



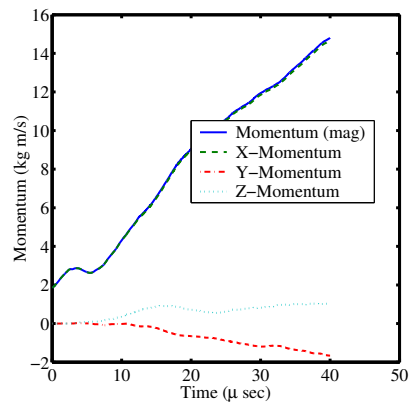
(a) Multiplier = 0.8



(b) Multiplier = 0.1

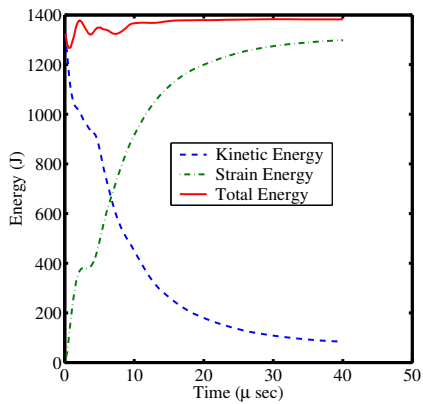


(c) Multiplier = 0.8

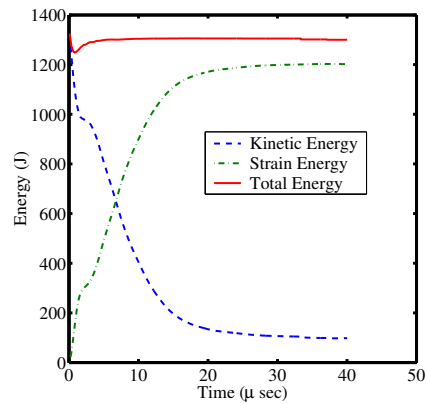


(d) Multiplier = 0.1

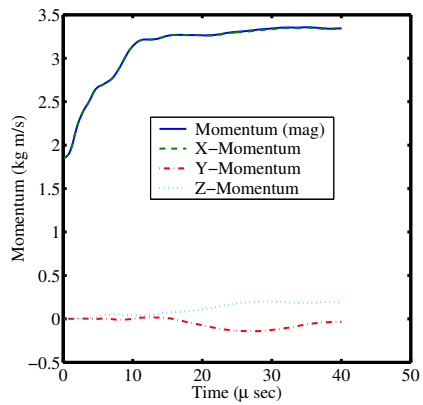
Figure 14: Energy and momentum balance for different timestep multipliers.



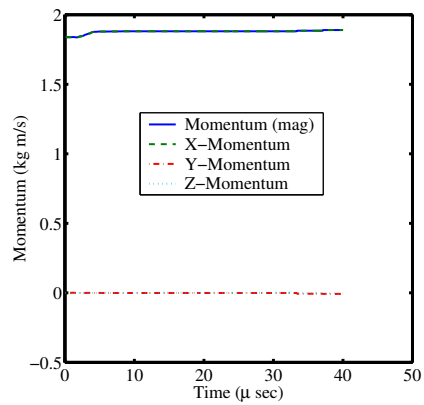
(a) friction contact.



(b) single\_velocity contact.

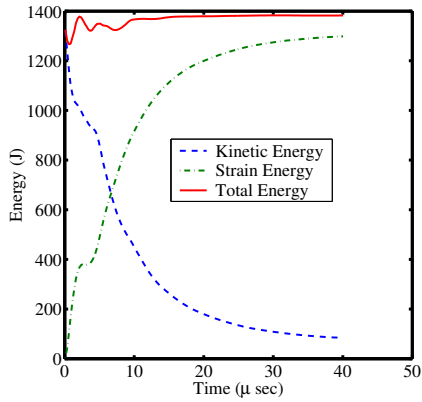


(c) friction contact.

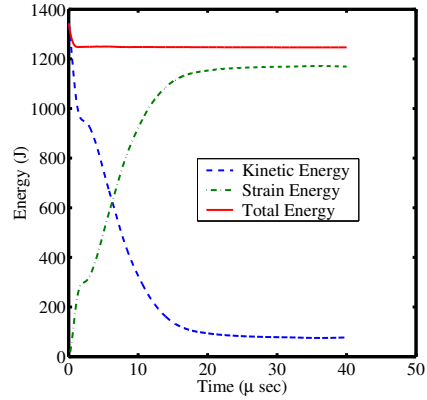


(d) single\_velocity contact.

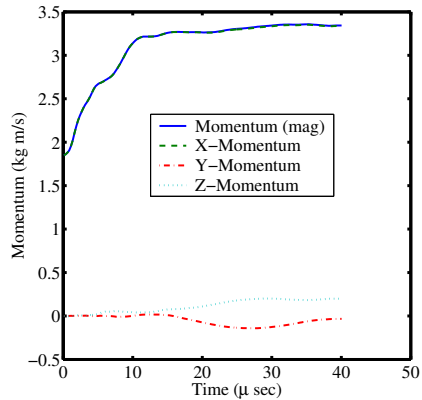
Figure 15: Energy and momentum balance for different contact algorithms.



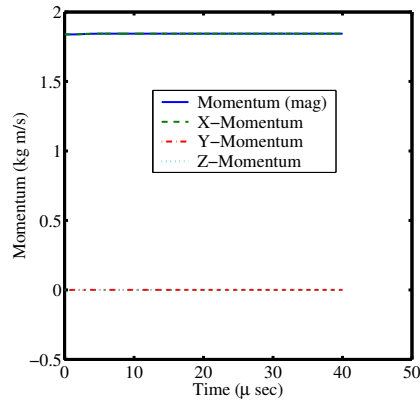
(a) friction contact + multiplier = 0.8.



(b) single\_velocity contact + multiplier = 0.1.



(c) friction contact + multiplier = 0.8.



(d) single\_velocity contact + multiplier = 0.1.

Figure 16: Energy and momentum balance for different contact algorithms and timestep multipliers.